

Cryo-EM structure of the BLOC-3 complex provides insights into the pathogenesis of Hermansky-Pudlak syndrome

Received: 4 July 2024

Accepted: 14 March 2025

Published online: 26 March 2025

Xin Yong^{1,5}, Guowen Jia^{2,5}, Qin Yang^{1,5}, Chunzhuang Zhou^{1,5}, Sitao Zhang¹, Huaqing Deng¹, Daniel D. Billadeau³, Zhaoming Su²✉ & Da Jia^{1,4}✉

Biogenesis of lysosome-related organelle complex-3 (BLOC-3) is pivotal in vesicle trafficking and has been linked to Hermansky-Pudlak syndrome (HPS). Despite its importance, the structure and molecular function of BLOC-3 remains elusive. Here, we report the Cryo-EM structure of human BLOC-3 at 3.2 Å resolution. The BLOC-3 complex consists of one copy of HPS1 and HPS4, which tightly associate with each other via their longin domains (LD1 and LD3). The unique four-helical bundle (4HB) domain of HPS1 is involved in stabilizing its LD1 and LD2 domains. Moreover, we identify interactions between BLOC-3 and the small GTPases RAB32/38 and RAB9A, which are essential for lysosome-related organelle biogenesis. Functional assays using zebrafish models confirm the significance of BLOC-3 assembly and its interaction with RAB9A during melanosome biogenesis. Most importantly, our structural information provides an accurate prediction for clinical variants associated with HPS. In summary, our study provides a comprehensive understanding of the molecular architecture and functional roles of BLOC-3, shedding light on HPS pathogenesis.

Hermansky-Pudlak syndrome (HPS) is a group of rare autosomal recessive disorders with limited treatment options, characterized by diminished vision, oculocutaneous albinism (reduced skin and hair pigmentation) and bleeding tendencies, often accompanied by pulmonary fibrosis and granulomatous colitis^{1–3}. These symptoms arise from dysfunctions in various lysosome-related organelles (LROs), specialized membrane-bound organelles with cell type-specific functions, including melanosomes in melanocytes, dense granules in platelets, lamellar bodies in alveolar type II (AT2) cells, et al.^{1,4}. Although HPS is rare in the general population (with an estimated incidence of 1:1,000,000), it exhibits high prevalence in certain populations and regions, such as an estimated occurrence of ~1:1800 individuals in Puerto Rico².

Genetic investigations have revealed that HPS stems from mutations in any of 10 genes in humans and 16 genes in mice, which encode proteins that form multiple protein complexes, including biogenesis of lysosome-related organelles complex-1, -2, and -3 (BLOC-1, -2, and -3)^{1,5–8}. The BLOCs are expected to mediate vesicle trafficking in the biogenesis of LROs, but their precise molecular functions remain poorly understood. BLOC-3 consists of two proteins known as HPS1 and HPS4, mutations in which give rise to the most common and severe subtypes of HPS. Mutations in HPS1 are the predominant cause of HPS, accounting for approximately 50% of HPS cases globally, whereas mutations in HPS4 are associated with around 12% of HPS cases worldwide^{1,9}. Remarkably, over 2000 genetic variants in these

¹Key Laboratory of Birth Defects and Related Diseases of Women and Children, Department of Paediatrics, West China Second University Hospital, State Key Laboratory of Biotherapy and Collaborative Innovation Center of Biotherapy, Sichuan University, Chengdu, China. ²State Key Laboratory of Biotherapy, Department of Geriatrics and National Clinical Research Center for Geriatrics, West China Hospital, Sichuan University, Chengdu, China. ³Division of Oncology Research and Schulze Center for Novel Therapeutics, Mayo Clinic, Rochester, USA. ⁴Development and Related Diseases of Women and Children Key Laboratory of Sichuan Province, West China Second University Hospital, Sichuan University, Chengdu, China. ⁵These authors contributed equally: Xin Yong, Guowen Jia, Qin Yang, Chunzhuang Zhou. ✉e-mail: zsulab2019@gmail.com; JiaDa@scu.edu.cn

two genes have been documented in the ClinVar database (<https://www.ncbi.nlm.nih.gov/clinvar>), and most of them are of uncertain clinical significance^{10,11}. It is challenging to determine whether these variants are pathogenic or not, due to limited diagnostic methods.

BLOC-3 serves as the guanine nucleotide exchange factor (GEF) for two highly related small GTPases, RAB32 and RAB38¹². In addition to the biogenesis of LROs, both BLOC-3 and RAB32 are also indispensable for immune responses against bacterial and fungal intracellular pathogens^{13–17}. Moreover, BLOC-3 functions as the effector of the small GTPase RAB9A¹⁸, and RAB9A likely also contributes to the biogenesis of LROs^{19,20}. However, it remains elusive how the BLOC-3 complex is assembled, and how BLOC-3 cooperates with RAB9A and RAB32/38 to regulate the biogenesis of LROs.

Both HPS1 and HPS4 belong to the Tri Longin Domain (TLD) RabGEF family, and each contains three longin-like domains (LDs) (Fig. 1a and b). TLD RabGEFs typically consist of at least two subunits, each containing three LDs (Fig. 1a). Alongside BLOC-3, TLD RabGEFs include two other complexes, including the Rab7 GEF Mon1-Ccz1 (in fungi) or Mon1-Ccz1-RMC1 (in metazoans), and the Rab23 GEF Fuzzy-Inturned-Wdpcp, also known as ciliogenesis and planar cell polarity effector complex (CPLANE)^{21–24}. Unlike Mon1 and Ccz1, which are evolutionarily conserved in all surveyed eukaryotic organisms (Fig. 1a), the subunits of BLOC-3 and CPLANE are missing in unicellular eukaryotes (Fig. 1a). Recent structural studies have significantly advanced our understanding of the molecular functions and assembly mechanism of Mon1-Ccz1-RMC1^{21,24} and CPLANE²³. However, the structural information of BLOC-3 is still lacking.

In this study, we determine the near-atomic resolution structure of BLOC-3 using single-particle cryo-electron microscopy (cryo-EM). The BLOC-3 structure also provides a framework to understand its interaction with RAB32/38 or RAB9A. Using the zebrafish model, we demonstrate that the BLOC-3 assembly and its interaction with RAB9A are crucial for the biogenesis of melanosomes. Finally, our structure successfully explains almost all known pathogenic HPS mutations occurring on HPS1 and HPS4. Altogether, our studies offer valuable insights into the assembly and molecular functions of the BLOC-3 complex during the pathogenesis of HPS.

Results

Reconstitution of the human BLOC-3 complex

To elucidate the assembly mechanism of the BLOC-3 complex, we initially co-expressed and purified *Homo sapiens* (Hs) HPS1 and HPS4 full-length proteins (HPS1-HPS4^{FL}) in insect cells using a baculovirus expression system (Fig. 1b, c). Preliminary cryo-EM analysis of HPS1-HPS4^{FL} revealed preferred orientation. To overcome this problem, we deleted a disordered region within the LD2 domain of HPS4 (HPS4Δ289–518, HPS4^{Δloop}), which resulted in the HPS1-HPS4^{Δloop} complex with improved yield and increased stability (Fig. 1c). The eluted HPS1-HPS4^{Δloop} from size exclusion column exhibited an estimated mass of 140 kDa, consistent with the size of a complex containing one copy of each subunit (Fig. 1c).

The purified HPS1-HPS4^{Δloop} exhibited improved monodispersed particles on the cryo-EM grids, enabling us to achieve a three-dimensional (3D) reconstruction of the complex at 3.2 Å global resolution (Fig. 1d, e, Table 1 and Supplementary Fig. 1). The map facilitated the construction of a model encompassing all LD domains, as well as the four-helical bundle (4HB) domain of HPS1, revealing detailed interactions between HPS1 and HPS4 (Fig. 1d, e, Table 1 and Supplementary Fig. 1). Several loops were not resolved in the map, likely due to their high flexibility.

Structural comparison of BLOC-3 with Mon1-Ccz1-RMC1 and CPLANE

HPS1 and HPS4 each harbor three LDs. The LD1, LD2, and LD3 of HPS1 and HPS4 adopt a canonical longin fold, a roadblock longin-like fold, and

a lamtor longin-like fold, respectively^{25,26} (Figs. 1d, e, 2a). Notably, in both HPS1 and HPS4, these LD domains are arranged in a triangular configuration, with each domain establishing contacts with the other two (Figs. 1d, e, 2a). HPS1 contacts HPS4 mainly through their LD1 and LD3 domains (Figs. 1d, e, 2a). Analogous LD configurations and interactions have been observed in two other TLD RabGEF complexes, the Mon1-Ccz1-RMC1 complex^{21,24} and the CPLANE complex²³. Each of these complexes comprises two TLD RabGEF family proteins (HPS1 and HPS4 in BLOC-3, Mon1 and Ccz1 in Mon1-Ccz1-RMC1, or Inturned and Fuzzy in CPLANE), while Mon1-Ccz1-RMC1 and CPLANE also feature a non-TLD protein with similar structural domains (RMC1 in Mon1-Ccz1-RMC1, or Wdpcp in CPLANE) bound to the TLD proteins (Fig. 2b and c). The TLD proteins of the BLOC-3, Mon1-Ccz1-RMC1 and CPLANE complexes share low protein sequence similarity (Supplementary Fig. 2). Structural comparison conducted using the DALI protein structure comparison server (<http://ekhidna2.biocenter.helsinki.fi/dali/>) indicate that HPS1 is more similar to Mon1 and Fuzzy, whereas HPS4 more closely related to Ccz1 and Inturned (Supplementary Fig. 2).

A pairwise comparison of LD1s, LD2s, and LD3s reveals that the structures of these domains in HPS1, HPS4, Mon1, Ccz1, Inturned and Fuzzy exhibit high similarity (Fig. 2d–i). All LDs share the basic Longin fold, characterized by a central five-stranded antiparallel β-sheet with conserved topology, two α-helices on one side of the sheet, and a single α-helix on the opposite side²² (Fig. 2d–i). Unlike LD1s and LD2s, LD3s lack one helix, and one helix (αx) between LD1 and LD2 is supplied to complete the longin fold (Fig. 2d–i and Supplementary Figs. 3, 4).

Despite their shared characteristics, the LD structures of HPS1 and HPS4 diverge from those of Mon1, Ccz1, Inturned, and Fuzzy in several aspects (Fig. 2d–i). First, LD1 and LD2 of HPS1 harbor two additional α-helices (LD1-α1 and LD1-α4) and β-strands (LD2-β4 and LD2-β5), compared to other LD1s and LD2s (Fig. 2d and Supplementary Fig. 5). Among them, LD1-α4 and LD2-β3 stack against the unique 4HB domain of HPS1 (Fig. 2d and Supplementary Figs. 5 and 6). Second, the LD3 domain of HPS1 features a unique loop (LoopA) and a following α-helix (LD3-α3) between LD3-β4 and LD3-β5, distinguishing it from other TLD RabGEF proteins (Fig. 2d–i). Last, the LD3 domain of HPS4 presents an extended loop (LoopB) situated between LD3-β5 and LD3-α2, which is also unique among all TLD RabGEF proteins (Fig. 2e). Interestingly, many unique structural elements of HPS1 and HPS4 are involved in their contacts, indicating a different assembly mechanism between HPS1 and HPS4 relative to other TLD RabGEF family members.

The 4HB domain is unique to HPS1, but not found in other TLD proteins. DALI search reveals that the 4HB domain of HPS1 exhibits similarities with many other four-helix bundle proteins, such as lipid droplet protein TIP47/PLIN3^{27,28} (root-mean-square-deviation (r.m.s.d) of 3.2 Å for 98 aligned Cα atoms, Supplementary Fig. 7), and apolipoproteins like apolipoprotein E (apoE)²⁹ (r.m.s.d of 3.3 Å for 95 aligned Cα atoms, Supplementary Fig. 7). However, careful structural examination indicates that the 4HB domain of HPS1 does not possess key structural elements of apoE, such as the aspartate binding pocket of apoE²⁹ (Supplementary Fig. 7). The local resolution of BLOC-3 (Supplementary Fig. 1b) shows that the 4HB region has lower resolution than the rest of the complex, suggesting that the 4HB domain is more flexible.

Assembly mechanism of the BLOC-3 complex

Similar to Mon1-Ccz1 and Fuzzy-Inturned, the HPS1-HPS4 interface is formed by LD1-LD1 and LD3-LD3. However, the HPS1-HPS4 interface (~2425 Å²) is significantly larger than those of Mon1-Ccz1 (~1715 Å²) and Fuzzy-Inturned (~1898 Å²). The interaction between HPS1 and HPS4 involves hydrogen bonds, salt bridges, and extensive hydrophobic interactions (Fig. 3a, b). Importantly, many interface residues are highly conserved in different organisms (Fig. 3a, b).

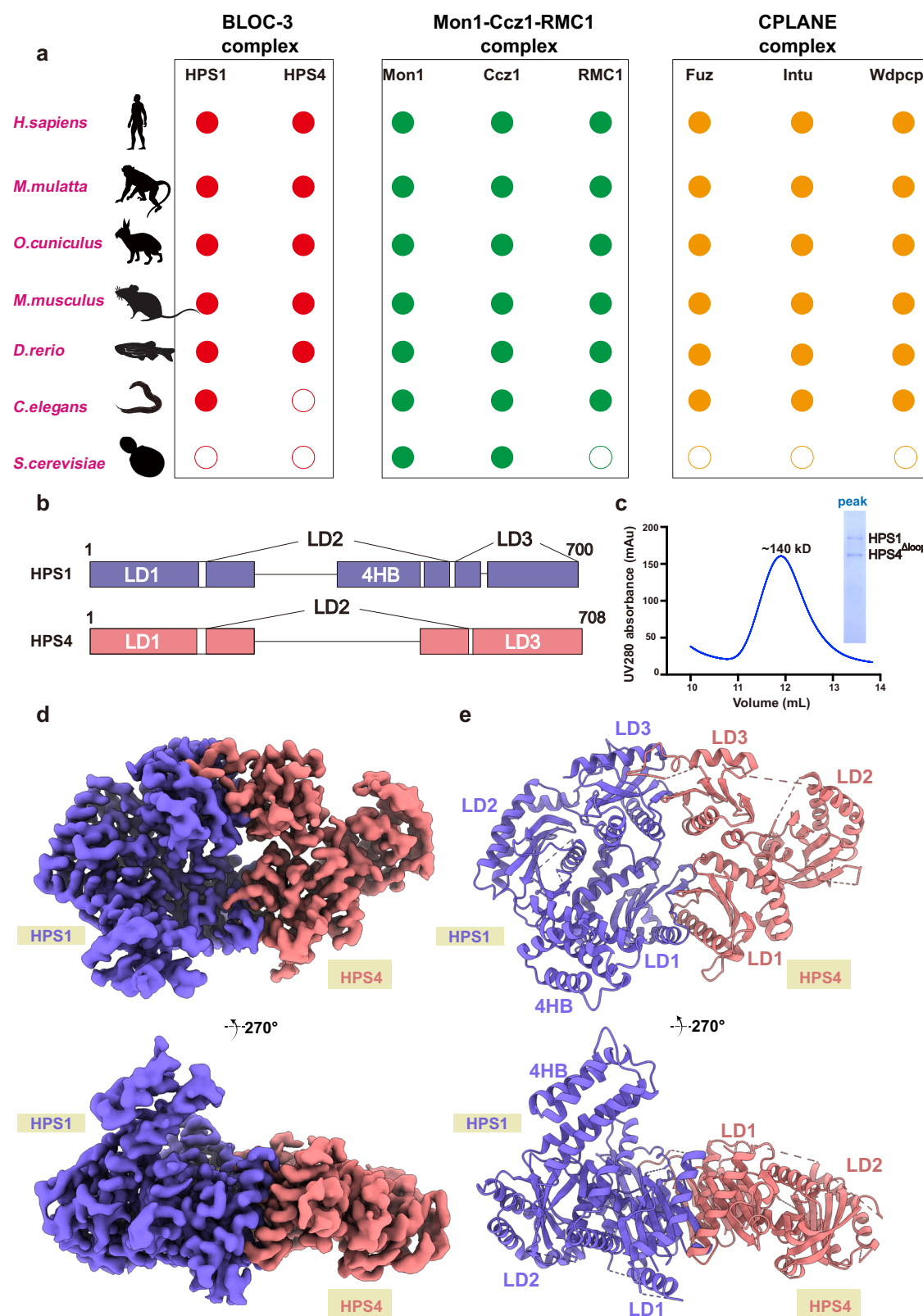


Fig. 1 | Cryo-EM structure of the BLOC-3 complex. **a** Cartoon representation incorporating the results of multiple phylogenetic analyses, including subunits from BLOC-3, Mon1-Ccz1-RMC1, and CPLANE, respectively. **b** Schematic domain organization of human BLOC-3 subunits. Longin domains (LD1 to LD3) and four-helical bundle domains (4HB) are indicated. **c** Gel filtration profile of the BLOC-3 complex. The horizontal axis represents elution volume, and the vertical axis

represents ultraviolet (UV) absorption. The peak and estimated molecular mass of targeted proteins are labeled. The Coomassie blue-stained gel shows the peak fraction of HPS1-HPS4^{Δloop} from gel filtration. **d**, **e** Two views of the cryo-EM density (left) and model (right) of the BLOC-3 complex. HPS1 is shown in purple, and HPS4 in pink. The bottom view is a 270° rotation along the horizontal axis of the top view.

Table 1 | . Cryo-EM map and model statistics, Related to Figs. 1, 3 and 5

Data collection and processing	BLOC3 complex	HPS1-HPS4-Rab9A Q66L complex
Magnification	165,000	
Voltage (kV)	300	
Pixel size (Å)	0.85	
Symmetry imposed	C1	
Micrographs acquired	10,755	11,110
Electron exposure (e ⁻ /Å ²)	52.1	61.6
Defocus range (μm)	−3.0 ~ −0.1	−5.5 ~ −0.1
Initial particle images (no.)	1,118,353	851,793
Final particle images (no.)	213,712	93,089
Map resolution (Å)	3.19	4.4
FSC threshold	0.143	0.143
Map resolution range (Å)	3.1 ~ 5.1	3.5 ~ 6.4
Model refinement		
Model resolution (Å)	3.5	N/A
FSC threshold	0.5	N/A
Map sharpening B factor (Å ²)	−128	N/A
Model composition		
Non-hydrogen atoms	7608	N/A
Protein residues	949	N/A
B factor (Å ²)	−79.88	N/A
R.m.s. deviations		
Bond lengths (Å)	0.002	N/A
Bond angles (°)	0.516	N/A
MolProbity score	1.38	N/A
Clashscore	5.30	N/A
Ramachandran plot		
Favored (%)	9751	N/A
Allowed (%)	2.49	N/A
Outliers(%)	0.00	N/A

The LD1-LD1 dimer of BLOC-3 is highly analogous to that of Mon1-Ccz1 and Fuzzy-Inturned (Fig. 3c). In contrast, the LD3-LD3 dimer of BLOC-3 comprises three major interaction regions and sharply differs from that of Mon1-Ccz1 and Fuzzy-Inturned (Fig. 3d, e). Region 1 is formed by two β strands (HPS1 LD3-β3 and HPS4 LD3-β3) and adopts an architecture similar to its counterparts in Mon1-Ccz1 and Fuzzy-Inturned (Fig. 3d). Region 2 consists of two α-helices (HPS1 LD3-α2 and HPS4 LD3-α1) (Fig. 3c, d). A similar interaction is also found in Fuzzy-Inturned but absent in Mon-Ccz1. Specifically, L635 and E639 of HPS4 are embedded in the hydrophobic groove formed by the alkyl chains of L588, R591, Y592, and Y597 of HPS1 (Fig. 3d). In addition to the hydrophobic contacts, a hydrogen bond and a salt bridge are formed between HPS1 R591 and HPS4 E639 (Fig. 3d). Region 3 is formed by LD3-β3, LD3-β4, LD3-α4 and LoopA of HPS1 and LoopB from HPS4 and is completely missing in two other TLD RabGEF complexes (Fig. 3e). Region 3 is dominated by hydrophobic interaction formed by R678, S679, S680, F682, P683, P685, F690 of HPS4 LoopA and T599, F601, F612, W614, K622, Q624, M625, D678 and V681 in HPS1 (Fig. 3e). In addition to hydrophobic contacts, multiple hydrogen bonds (R678 of HPS4 and Q624 of HPS1; S679 of HPS4 and M625 of HPS1) are also observed (Fig. 3e).

To validate the structure, we mutated several key HPS1 residues in the interface: LD3-α2 (R591E/Y592A, RY), LoopA (K622E/Q624A, KQ), and LD3-α4 (D678R/V681A, DV). We also introduced two additional mutations in LD3-α2, L588A, and L588P, the latter of which was

identified in an HPS1 patient. While GFP-tagged HPS1 wild-type (WT) robustly retained HPS4, the L588P mutant failed to interact with HPS4, and the other four mutants dramatically decreased the binding to HPS4 (Fig. 3f, g). Similarly, we found that replacing residues from 675 to 686 with Gly/Ser linkers (675–686^{GS}) or deleting LoopB (Δ675–686) in HPS4 almost completely abolished its interaction with HPS1 (Fig. 3h, i). These results confirm our structural observations and indicate that disruption of complex assembly may contribute to the pathogenesis of HPS.

Conserved guanine nucleotide exchange mechanism by TLD RabGEFs

To characterize the GEF activity of BLOC-3, we loaded RAB38 with the fluorescent GDP analog MANT-GDP and examined the guanine nucleotide exchange rate with or without purified BLOC-3 (Fig. 4a). Purified HPS1-HPS4^{FL} increased the guanine nucleotide exchange rate of RAB38 in a concentration-dependent manner (Fig. 4a, b, and Supplementary Fig. 8). The catalytic efficiency of HPS1-HPS4 (k_{cat}/K_M $1.294 \pm 0.1640 \times 10^4 \text{ M}^{-1}\text{s}^{-1}$) is comparable with those of Mon1-Ccz1 and Fuzzy-Inturned^{30,31}. Critically, the HPS1-HPS4^{Δloop} complex showed a similar catalytic efficiency (k_{cat}/K_M $1.312 \pm 0.2266 \times 10^4 \text{ M}^{-1}\text{s}^{-1}$) to that of HPS1-HPS4^{FL} (Fig. 4b).

To gain additional insights into the binding and catalytic mechanism of BLOC-3, we modeled the interaction between BLOC-3 and RAB38 using AlphaFold³² (Fig. 4c, d, and Supplementary Fig. 9a, b). The predicted HPS1-HPS4-RAB38 binding is highly similar to that of Mon1-Ccz1-YPT7³⁰ (a yeast homolog of human RAB7A, Supplementary Fig. 9a–e). The main interface is composed of two α-helices from HPS1 (LD1-α2) and HPS4 (LD1-α1), along with switch I in RAB38 (Fig. 4c, d). An overlay of the HPS1-HPS4-RAB38 model with the crystal structure of RAB38 in complex with GTP (RAB38-GTP)³³ indicate that HPS1-HPS4 leads to a dramatic remodeling of the nucleotide-binding pocket of RAB38 (Fig. 4c, d). Specifically, the entire switch I becomes ordered, and Y38 from the switch I of RAB38 inserts into a hydrophobic pocket in the LD1 heterodimer surface of HPS1-HPS4 (Fig. 4d). Remarkably, the conformation imposed by HPS1-HPS4 allows RAB38 R39 to insert into the nucleotide-binding pocket (Fig. 4d). RAB38 R39 is surface-exposed and disordered in the GTP-bound state; in contrast, R39 occupies the position of Mg²⁺ ion in the nucleotide-bound structure in the presence of HPS1-HPS4, thereby destabilizing nucleotide binding.

To test above hypothesis, we substituted Y38 and R39 in RAB38 (or Y54 and R55 in RAB32) with leucine or alanine, respectively, and performed GEF activity assay in the presence of the purified HPS1-HPS4^{Δloop} complex (Fig. 4e, f, and Supplementary Fig. 10). We did not use a pull-down assay as the interaction between BLOC-3 and RAB32/38 is known to be weak and transient. HPS1-HPS4^{Δloop} effectively promoted the guanine nucleotide exchange of RAB38 WT; in contrast, its catalytic efficiency was significantly reduced when RAB38 Y38L or R39A were used (Fig. 4e and Supplementary Fig. 10a–c). Similarly, both Y54 and R55 of RAB32 were also critical for the GEF activity of HPS1-HPS4^{Δloop} (Fig. 4f and Supplementary Fig. 10d–f).

Interestingly, Y38R39 of RAB38 and Y54R55 of RAB32 are conserved in all TLD RabGEF complex-associated RabGTPases, including RAB7A and RAB23 (Fig. 4g). This motif, consisting of a tyrosine followed by an arginine or lysine residue, is referred to as the Y[R/K] motif from here on. The Y[R/K] motif is completely missing in other Rab GTPases that we surveyed, indicating that TLD RabGEFs may activate their substrates via this motif (Fig. 4g). Consistent with our hypothesis, Kiontke et al.³⁰ found that Y37 and K38 of Ypt7 (corresponding to Y38 and R39 in RAB38 or Y54 and R55 in RAB32) were critical for the catalytic activity of Mon1-Ccz1. Thus, we propose that RAB7A, RAB23, RAB32, and RAB38 utilize the conserved Y[R/K] motif to associate with their respective TLD RabGEFs.

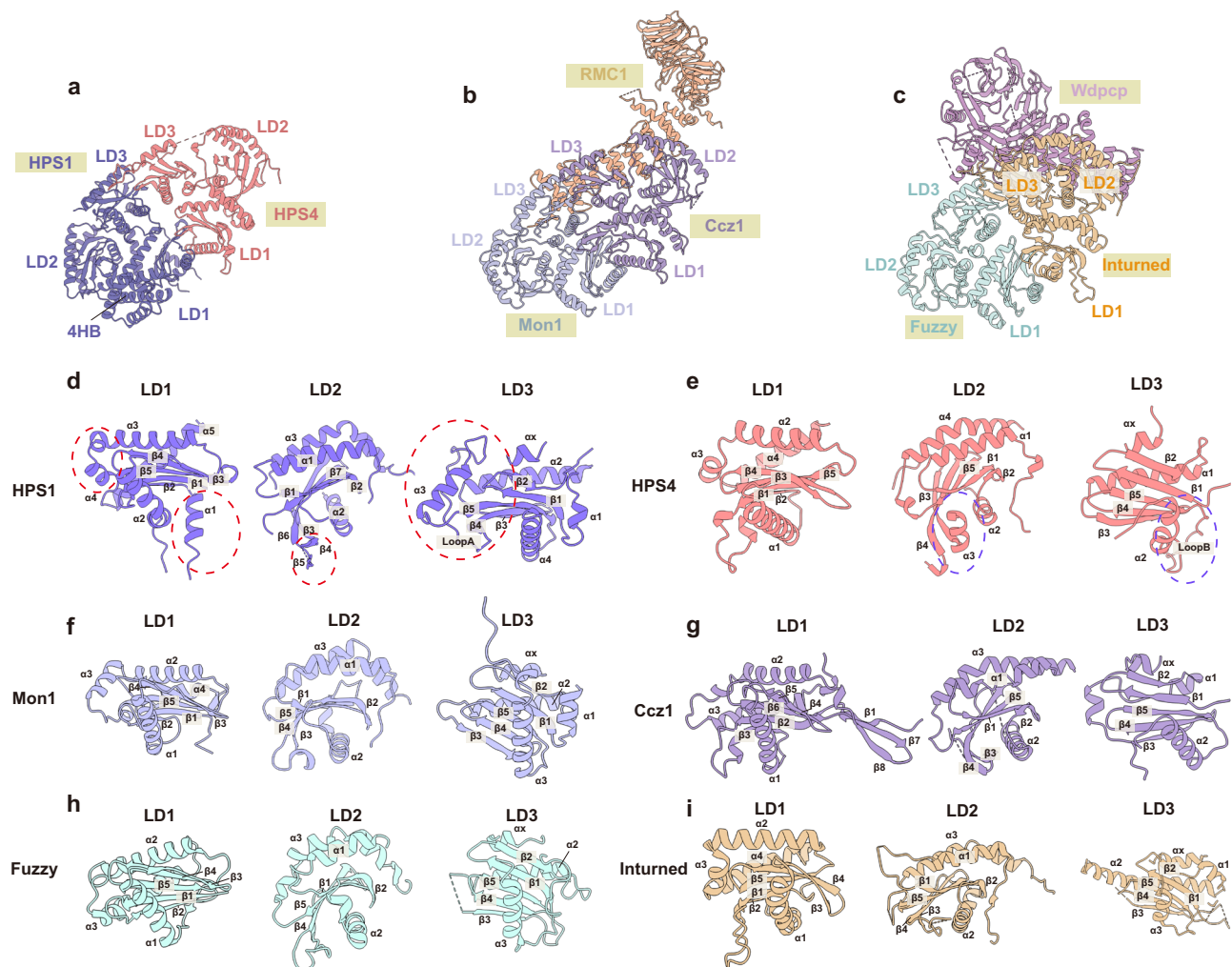


Fig. 2 | Structural comparison of BLOC-3, Mon1-Ccz1-RMC1 and CPLANE. a–c Cyro-EM structures of BLOC-3, Mon1-Ccz1-RMC1 (PDB: 8JBE), and CPLANE (PDB: 7Q3D). d–i Closeup view of the LD domains from TLD RabGEF proteins.

Secondary structures of TLD RabGEF proteins are labeled as indicated. The unique structures of LD domains from HPS1 and HPS4 are highlighted in circles.

Binding mechanism between BLOC-3 and RAB9A

BLOC-3 is an effector of RAB9A, and the Rab9–BLOC-3 axis is likely to be involved in melanogenesis^{15,18–20}. To gain insights into the binding between RAB9A and BLOC-3, we purified BLOC-3 in complex with mouse Rab9A Q66L, a GTP-bound constitutively active mutant, which co-eluted from the size exclusion chromatography (Supplementary Fig. 11a). Unfortunately, the BLOC-3-Rab9A complex tended to dissociate upon sample freezing. As a result, we could only determine the structure of the BLOC-3-Rab9A complex at an averaged resolution of ~4.4 Å, and the local resolution of Rab9A was even lower (Fig. 5a, and Supplementary Fig. 11b, c). To overcome the problem, we modeled the interaction between human BLOC-3 and RAB9A, including the GTP ligand, using AlphaFold3³⁴ (Fig. 5b, and Supplementary Figs. 11, 12). The predicted model aligned well with the low-resolution 3D cryo-EM envelope (Fig. 5a). Previous studies^{23,35} suggest that Mon1 and Fuzzy directly interact with RAB5 and Rsg1 in Mon1-Ccz1-RMC1 and CPLANE (Supplementary Fig. 13). In contrast, our model indicates that in BLOC-3, HPS4, which is more closely related to Ccz1 and Inturned, is directly involved in binding to RAB9A (Fig. 5a, b and Supplementary Fig. 13).

In our model, RAB9A is positioned at the end of the HPS1-HPS4 heterodimer and interacts exclusively with the LD2 domain of HPS4 (Fig. 5a). In this interaction, the switch and interswitch regions of RAB9A assume an active conformation akin to that in the GppNHp-bound RAB9A, consistent with the notion that BLOC-3 functions as an

effector of RAB9A. A comparison of the predicted RAB9A-BLOC-3 structure and the crystal structure of RAB9A with its effector RUTBC2³⁶ offers some interesting insights. Although RAB9A uses a similar region (switch I, switch II, and interswitch) to contact HPS4 or RUTBC2, HPS4 or RUTBC2 adopts distinct structures. Specifically, RUTBC2 employs two β strands and one short α-helix to contact RAB9A³⁶, whereas HPS4 utilizes two α-helices (LD2-α1 and LD2-α4) (Fig. 5b).

The AlphaFold3-derived model, together with sequence alignment of HPS4, indicate that four surface-exposed residues from the LD2 domain of HPS4, K175, R178, S578, and N580, may engage with switch I and interswitch region of RAB9A (Fig. 5b and Supplementary Fig. 4). To assess the prediction, we generated two HPS4 mutants (K175A/R178A, KR and S578A/N580A, SN) and evaluated their binding ability to mouse Rab9A Q66L (Fig. 5c, d). Whereas HPS4 WT efficiently retained Rab9A Q66L, both HPS4 mutations markedly reduced the interaction with Rab9A Q66L (Fig. 5c, d).

Mapping the disease-derived mutations on BLOC-3

HPS1 and HPS4 represent the most prevalent and severe HPS subtypes, comprising approximately 60% of HPS cases worldwide^{1,9}. Although many HPS1 and HPS4 genetic mutations have been found in individuals diagnosed with HPS, it is largely unknown how these mutations contribute to the pathogenesis of HPS^{10,11}. To understand how the mutations alter the functions of BLOC-3, we mapped all reported disease-

associated missense variants and multiple frameshift mutations occurring on the LD3 domains of human HPS1 and HPS4¹⁰ onto our BLOC-3 model (Fig. 6a). Of the 24 disease-related mutations (17 in HPS1

and 7 in HPS4), 20 are missense mutations, and 4 are frameshift mutations. Except for two missense mutations (G313S of HPS1 and R268K of HPS4) located in unresolved parts, the remaining 18 missense

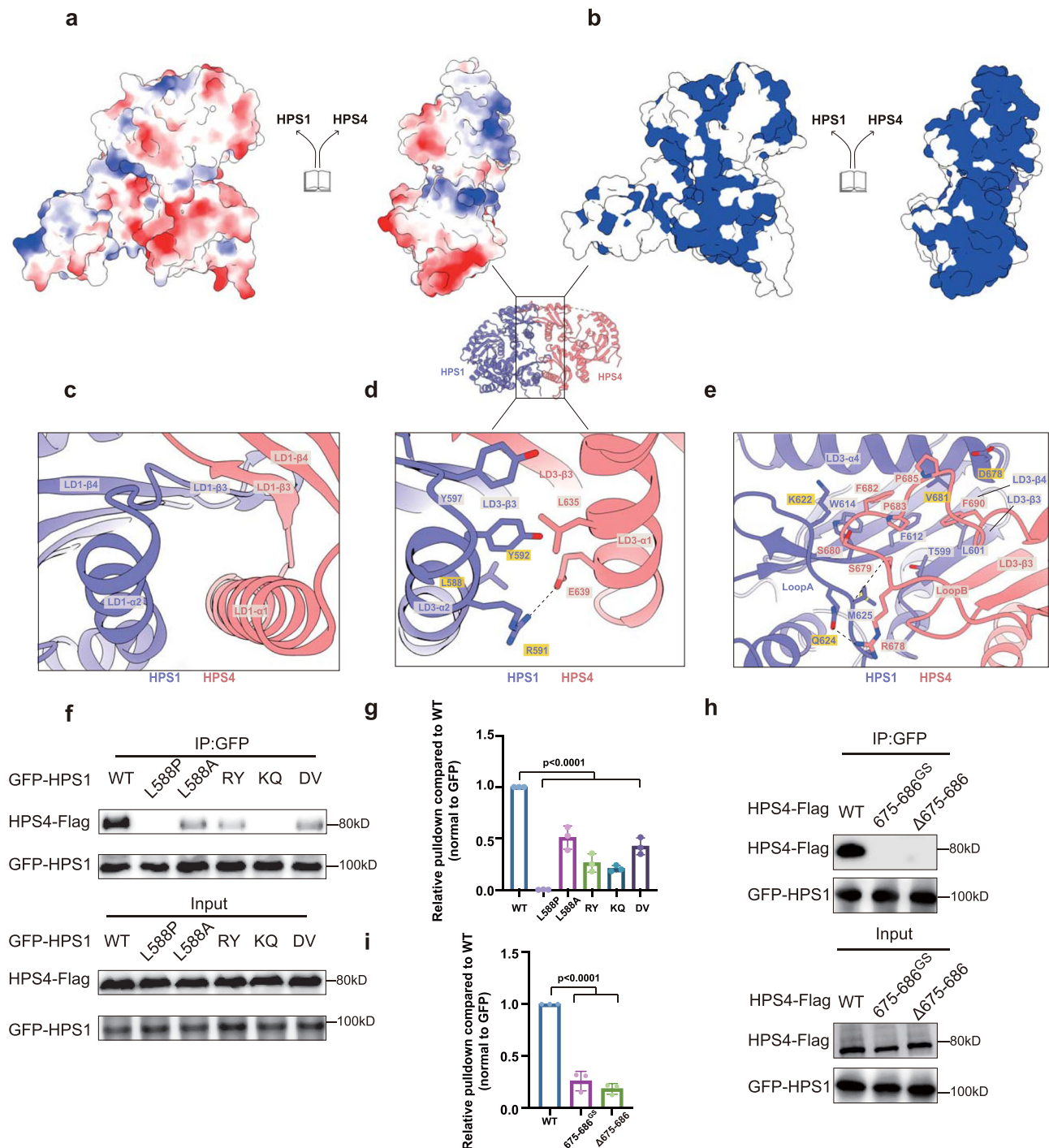


Fig. 3 | Comparative structural analysis reveals divergent assembly mechanisms of the BLOC-3 complex and other TLD RabGEFs. a, b Close-up views of the HPS1-HPS4 heterodimer interface illustrating electrostatic surface potential and conserved amino-acid residues (blue color represents conserved residues, while white color denotes non-conserved residues). **c-e** Detailed interactions of the interfaces between HPS1 (purple) and HPS4 (pink). Secondary structures of HPS1 and HPS4 are labeled as indicated. Residues critical for stabilizing the interface are shown in sticks. Black dashed lines indicate hydrogen bonds or salt bridges. Residues that are mutated in **(f)** are indicated with a yellow box. **(f)** HEK293T cells were transfected with Flag-tagged HPS4 and GFP-tagged HPS1 WT, L588P, L588A, R591E/Y592A(RY), K622E/Q624A(KQ), or D678R/V681A(DV) mutants, and subjected to

GFP-nanotrap for immunoprecipitation. HPS1 and HPS4 were detected via antibodies against GFP and Flag, respectively. **g** Quantification of the results presented in **(f)**. Statistical difference was determined by One-way ANOVA. Error bars represent the standard deviation of three independent biological repeats. $n = 3$. **h** HEK293T cells were transfected with GFP-tagged HPS1 and Flag-tagged HPS4 WT, 675-686^{GS} or Δ675-686 mutant, and subjected to GFP-nanotrap for immunoprecipitation. HPS1 and HPS4 were detected via antibodies against GFP and Flag, respectively. **(i)** Quantification of the results presented in **(h)**. Statistical difference was determined by One-way ANOVA. Error bars represent the standard deviation of three independent biological repeats. $n = 3$.

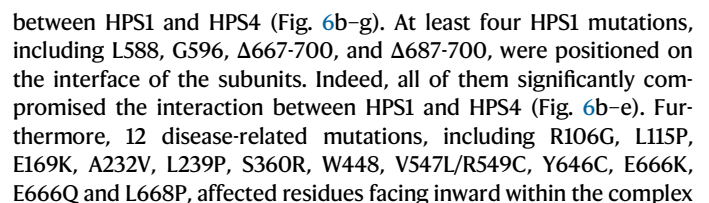


Fig. 4 | The conserved “Y[R/K]” motif in Rab GTPase switch I is required for their activation by TLD RabGEFs. **a** 2 μ M Mant-GDP-loaded GST-tagged RAB38 was added, and nucleotide exchange was triggered by adding 200 μ M GDP and 0, 0.125, or 0.25 μ M GEF complex. The decrease of fluorescence was measured over time and normalized to fluorescence prior to GEF addition. Error bars represent the standard error of the mean (SEM) from three technical replicates. $n = 3$. **b** Nucleotide exchange rates of HPS1-HPS4^{FL} and HPS1-HPS4^{Δloop} are plotted against the concentration of HPS1-HPS4, and the catalytic efficiency (k_{cat}/K_M) in $M^{-1}s^{-1}$ was determined as the slope of the linear fit to the equation $y = A \cdot x + B$. Error bars represent the SEM of three independent biological repeats. The catalytic efficiency (k_{cat}/K_M) of HPS1-HPS4^{FL} and HPS1-HPS4^{Δloop} is shown. $n = 3$. **c** Identification of the putative RAB32/38 binding site in BLOC-3. Model of the respective LD1 domain of HPS1 (purple) and HPS4 (pink), and RAB38 (green) complex based on an

AlphaFold2 prediction. **(d)** A zoom-in view of the HPS1-HPS4-RAB38 binding site superposed with the crystal structure of RAB38-GTP (magenta, PDB: 6hdu). HPS1 and HPS4 are shown in hydrophobic surface potential, and Y38 and R39 of RAB38 are shown in sticks. The predicted model is colored as in **(c)**. **e, f** Nucleotide exchange rates of RAB38 and RAB32 are plotted against the concentration of HPS1-HPS4, and the catalytic efficiency (k_{cat}/K_M) in $M^{-1}s^{-1}$ was determined as the slope of the linear fit to the equation $y = A \cdot x + B$. Error bars represent the SEM of three independent biological repeats. The catalytic efficiency (k_{cat}/K_M) of HPS1-HPS4^{Δloop} towards RAB32, RAB38, and indicated mutants is shown. N.d., not determined. $n = 3$. **g** Sequence alignment of the switch I regions of Rab GTPases. The Y[R/K] motif is highlighted in red, with * indicating highly conserved residues and representing residues that are moderately conserved.

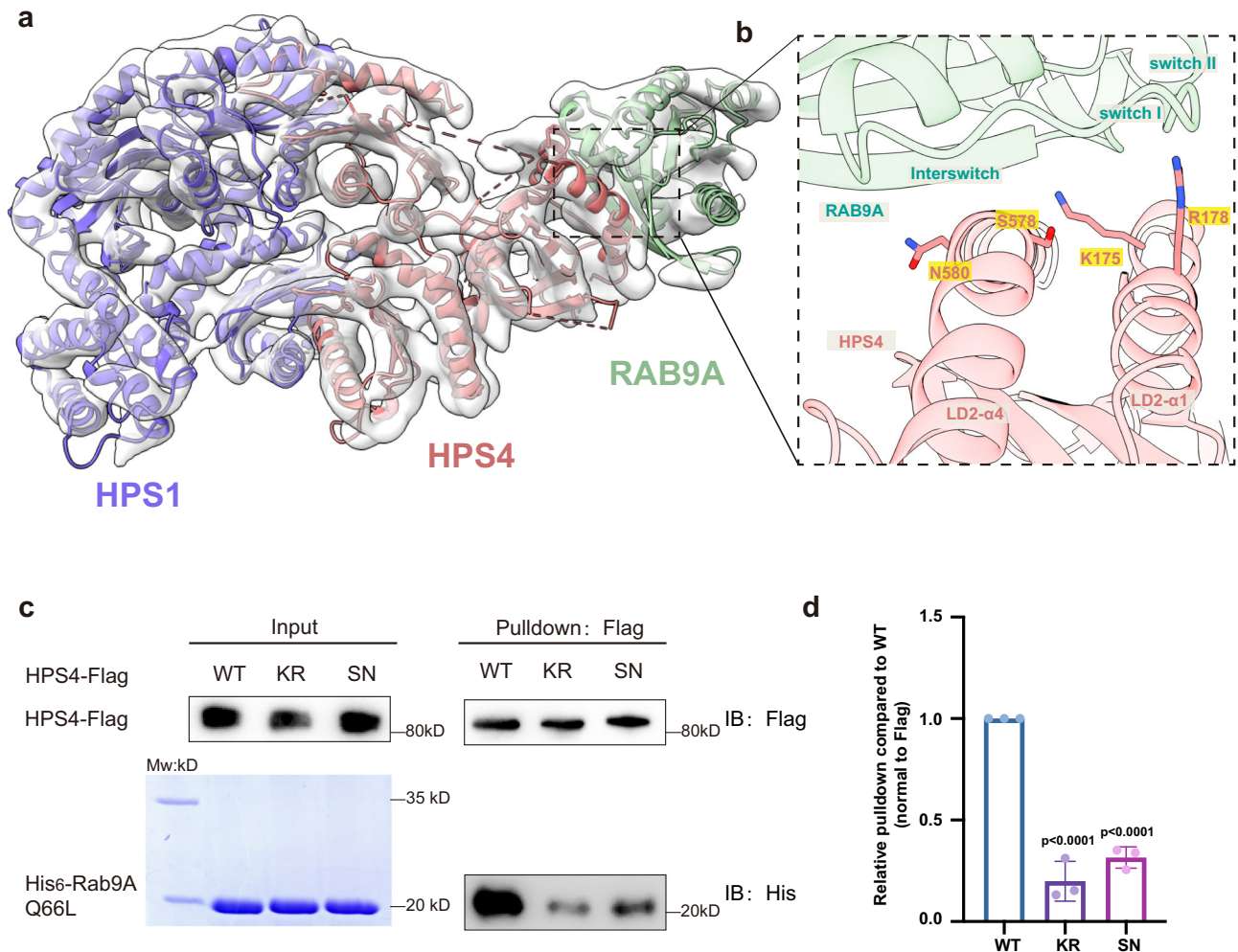


Fig. 5 | The interaction between BLOC-3 and RAB9A. **a** Low-resolution cryoEM envelope of BLOC-3-Rab9A Q66L with docked AlphaFold3 model. **b** Close-up view of the HPS4-RAB9A binding interface, with critical residues for RAB9A binding shown in sticks. Residues that are mutated in **(d)** are indicated with a yellow box. **c** Flag-tagged HPS4 WT and mutants were expressed and purified using

HEK293T cells, then incubated with purified His-tagged mouse Rab9A Q66L mutant and subjected to Flag pull-down. HPS4 and Rab9A were detected by antibodies against Flag and His, respectively. **d** Quantification of the results presented in **(c)**. Statistical differences were determined by One-way ANOVA. Error bars represent the standard deviation of three independent biological repeats. $n = 3$.

and impaired the assembly of the BLOC-3 complex (Fig. 6b–e). Among them, W448 resides in the third α -helix of the 4HB domain (4HB- α 3) and participates in interactions with three helices, and HPS1 W448R diminished interactions with HPS4 (Fig. 6b, c). Finally, although G313 is located within an unresolved loop between LD2- α 2 and LD2- β 3 in our structure, the G313S mutation still disrupted the interaction between HPS1 and HPS4 (Fig. 6b, c). This suggests that G313S might induce a conformational change or affect the overall stability of HPS1, thereby interfering with its interaction with HPS4.

Out of 7 disease-associated mutations in HPS4, two frameshift mutations (Δ 620-708, and Δ 631-708) affect residues in the HPS1-HPS4 interface (Fig. 6a). As expected, both significantly diminished the binding between HPS1 and HPS4 (Fig. 6f, g). Three additional HPS4 mutations, including L91P, H154R, and P619L, face inward in our structure and were found to reduce the binding between HPS1 and HPS4 (Fig. 6f, g). Last, R185 and R268 face outward in our structure, and their corresponding disease mutations, R185H, and R268K did not affect the interaction between HPS1 and HPS4 (Fig. 6f, g). R185H was

a

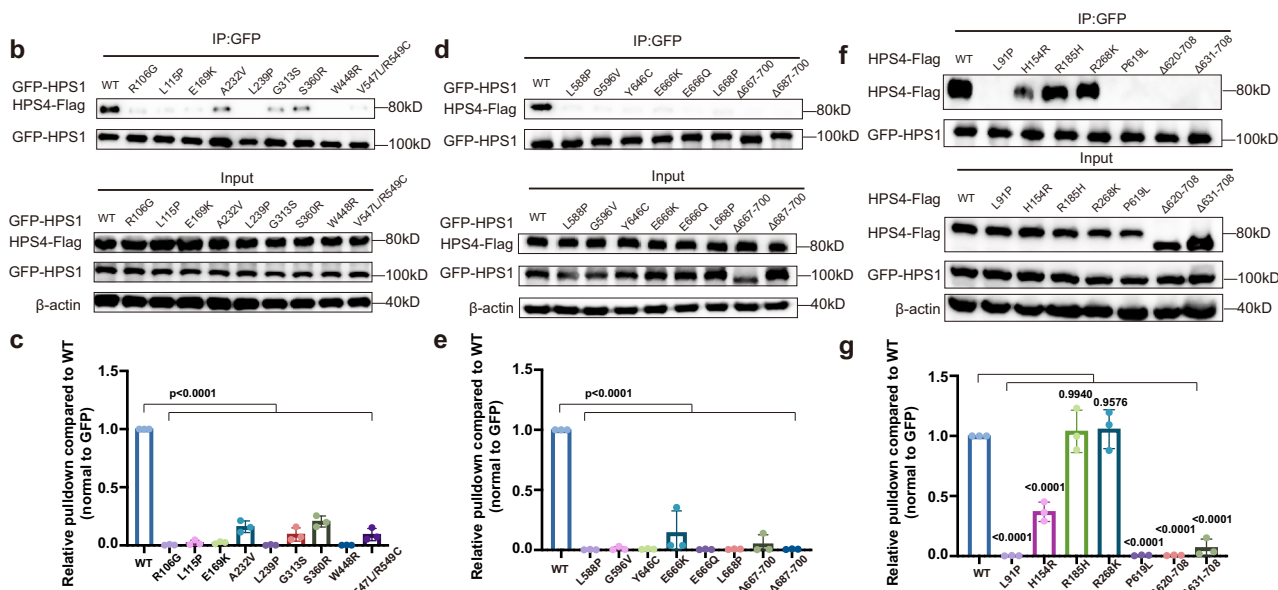
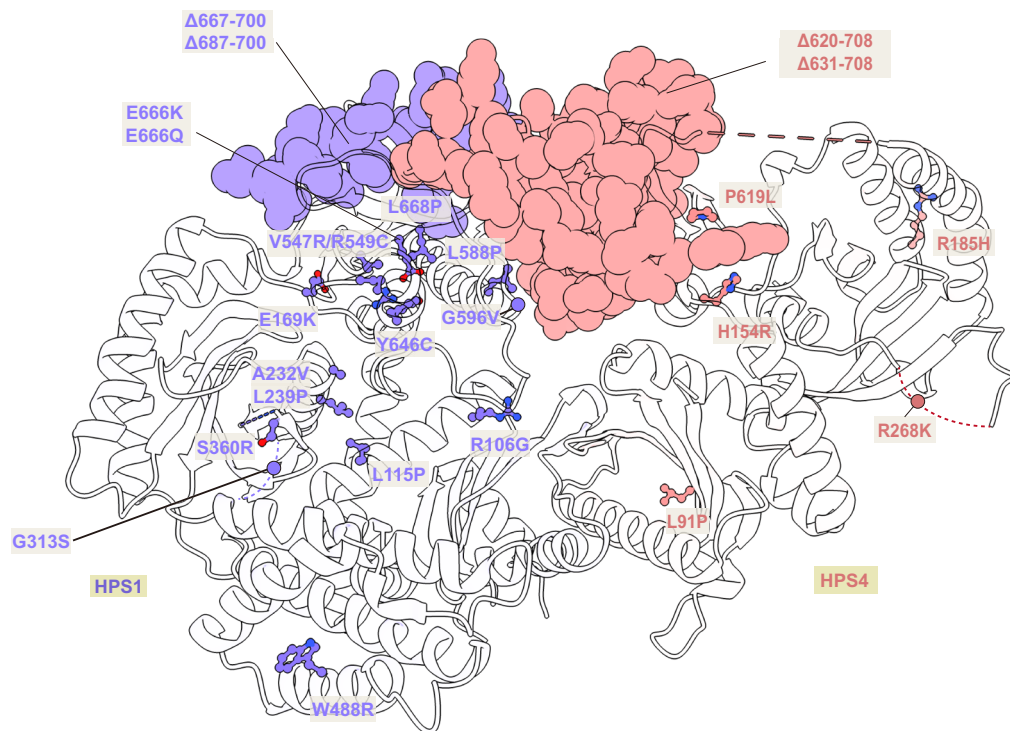


Fig. 6 | Structural mapping of the disease-related mutations and their effects on BLOC-3 assembly. **a** Structural mapping of the disease-associated mutations of BLOC-3. **b–e** Coimmunoprecipitation assays were used to assess the effects of the disease-associated mutations on the formation of BLOC-3. HPS1 mutation variants were cotransfected with Flag-tagged HPS4 in HEK293F cells, the cells were lysed and coimmunoprecipitated with anti-GFP affinity gel, and the purified samples and input samples were immunoblotted. Antibodies: anti-Flag (HPS4), anti-GFP (HPS1) and anti-β-Actin. **(c)** and **(e)** presented the quantification of the results presented in **(b)** and **(d)**, respectively. Statistical differences were determined by One-way

ANOVA. Error bars represent the standard deviation of three independent biological repeats. $n = 3$. **f, g** HPS4 mutation variants were cotransfected with GFP-tagged HPS1 in HEK293F cells, the cells were lysed and coimmunoprecipitated with anti-GFP affinity gel, and the purified samples and input samples were immunoblotted. Antibodies: anti-Flag (HPS4), anti-GFP (HPS1) and anti-β-Actin. **(g)** presented the quantification of the results presented in **(f)**. Statistical differences were determined by One-way ANOVA. Error bars represent the standard deviation of three independent biological repeats. $n = 3$.

identified as a likely damaging heterozygous variant in exon 7 of HPS4 (c.554 G > A)³⁸. However, experimental evidence is lacking whether R185H or R268K is pathogenic. In summary, our structural model provides a clear explanation for the majority of HPS variants (22 out of 24) identified in HPS1 or HPS4.

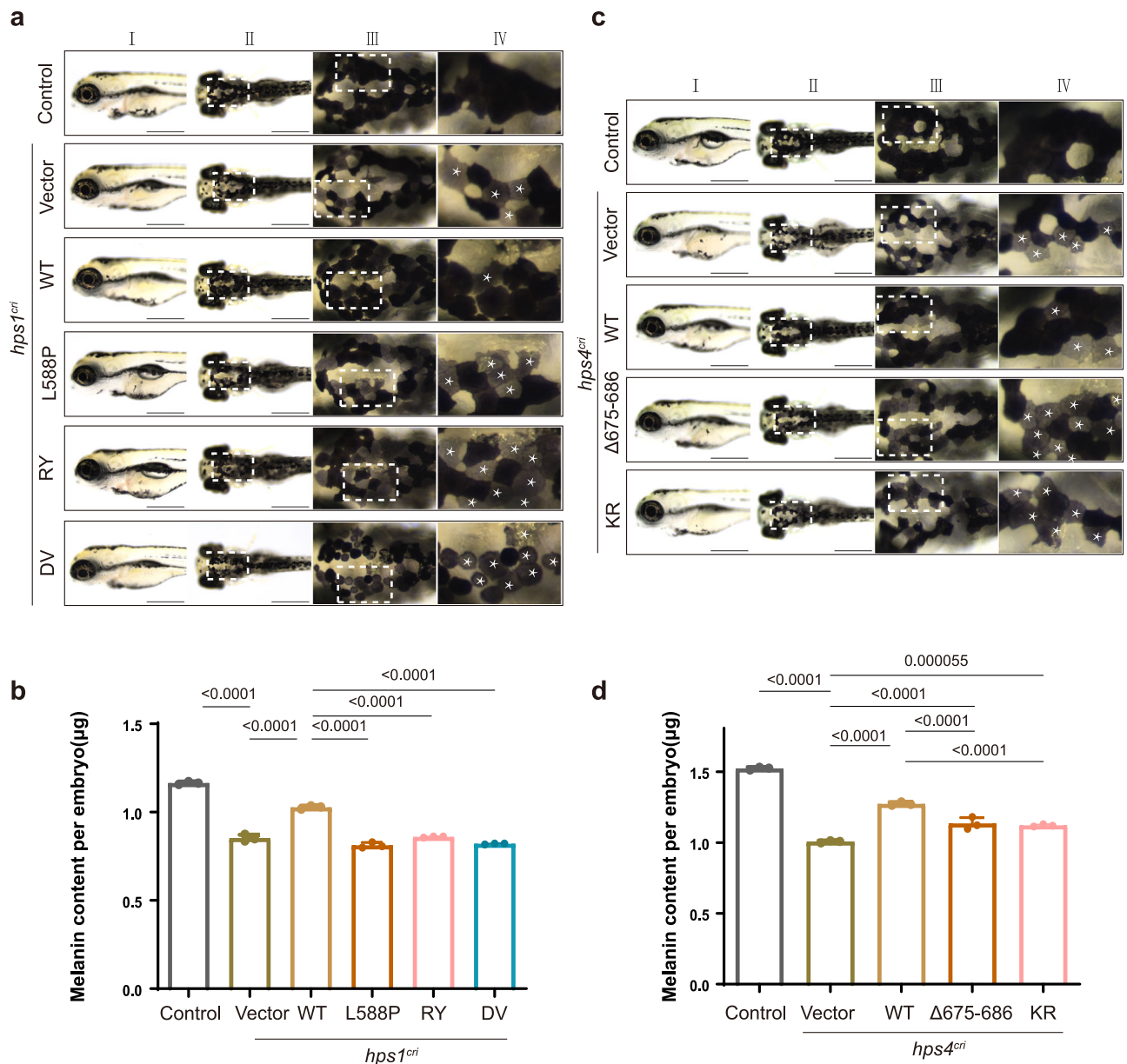


Fig. 7 | The interactions between HPS4 and HPS1 or RAB9A are critical for melanogenesis in zebrafish. a Bright-field images of zebrafish at 96 h post-fertilization (hpf). Scale bar, 500 μm. Column I, lateral view; column II, dorsal view; column III, zoomed-in view, corresponds to the white box of column II; column IV, zoomed-in view, corresponds to the white box of column III. White asterisks (*) indicate the putative affected cells. **b** The total melanin levels of zebrafish at 96 hpf. Control: control ribonucleoprotein complex (RNP) injection ($n = 35$ embryos), *hps1^{cri}*+vector: *hps1*-RNP and empty vector co-injection ($n = 32$ embryos), *hps1^{cri}* + WT: *hps1*-RNP and human HPS1-WT CDS plasmids co-injection ($n = 22$ embryos), *hps1^{cri}* + L588P: *hps1*-RNP and HPS1-L588P mutant CDS plasmids co-injection ($n = 35$ embryos), *hps1^{cri}* + RY: *hps1*-RNP and HPS1-RY mutant CDS plasmids co-injection ($n = 45$ embryos), *hps1^{cri}* + DV: *hps1*-RNP and HPS1-DV mutant CDS plasmids co-injection ($n = 29$ embryos). All injections were performed at the one-cell stage of development. Results were presented as mean \pm SD. P -values were

calculated using one-way ANOVA, Dunnett's multiple comparisons test. Experiments were repeated 3 times. **c** Bright-field images of zebrafish at 96 hpf. Scale bar, 500 μm. Column I, lateral view; column II, dorsal view; column III, zoomed-in view, corresponds to the white box of column II; column IV, zoomed-in view, corresponds to the white box of column III. White asterisks (*) indicate the putative affected cells. **d** The total melanin levels of zebrafish at 96 hpf. Control: control ribonucleoprotein complex (RNP) injection ($n = 40$ embryos), *hps4^{cri}*+vector: *hps4*-RNP and empty vector co-injection ($n = 34$ embryos), *hps4^{cri}* + WT: *hps4*-RNP and human HPS4-WT CDS plasmids co-injection ($n = 41$ embryos), *hps4^{cri}* + Δ675-686: *hps4*-RNP and HPS4 Δ675-686 mutant CDS plasmids co-injection ($n = 30$ embryos), *hps4^{cri}* + KR: *hps4*-RNP and HPS4-KR mutant CDS plasmids co-injection ($n = 25$ embryos). All injections were performed at the one-cell stage of development. Results were presented as mean \pm SD. P -values were calculated using one-way ANOVA, Dunnett's multiple comparisons test. Experiments were repeated 3 times.

HPS4 interactions with HPS1 and RAB9A are essential for melanogenesis in zebrafish

Genes encoding subunits of BLOC-1, BLOC-2, and BLOC-3 are conserved in zebrafish. Zebrafish with mutations or knockdowns of these genes displayed altered pigmentation^{1,39–45}. To assess the significance of interactions between HPS1-HPS4 and HPS4-RAB9A in melanogenesis, we chose zebrafish as our model organism (Fig. 7 and

Supplementary Fig. 14a–g). Using a CRISPR/Cas9-mediated F0 gene knockout system⁴⁶, we generated zebrafish crispants (F0 mutants) of *hps1* or *hps4* (Fig. 7 and Supplementary Fig. 14a–g). Consistent with the pivotal role of HPS1 and HPS4 in melanosome biogenesis, depletion of *hps1* or *hps4* altered melanosome structures in the retinal pigment epithelium^{42–44} (RPE, Supplementary Fig. 15a, b). Transmission electron microscopy (TEM) image analysis revealed that the average

melanosome circumference of *hps1* and *hps4* crispants was significantly smaller than that in the wild-type (Supplementary Fig. 15a, b). In addition, *hps1* and *hps4* crispants exhibited an increased number of multi-vesicular bodies, resembling partially pigmented stage III melanosomes (yellow arrowheads, Supplementary Fig. 15a).

Deletion of *hps1* led to a 27% decrease in melanin levels compared to control levels (Fig. 7a, b), while deletion of *hps4* resulted in a 34% reduction (Fig. 7c, d). Consistently, about 76.9% of *hps1* and 69.2% of *hps4* crispants exhibited melanogenesis deficiencies at 1 month post-fertilization (mpf) (Supplementary Fig. 15c, d). For convenience, we chose *hps1* and *hps4* crispants at 96 hpf for subsequent experiments. Critically, these defects could be restored to near wild-type levels when plasmid encoding human HPS1 or HPS4 was co-injected, suggesting that human HPS1 or HPS4 could compensate for the loss of zebrafish *hps1* or *hps4* (Fig. 7). In contrast, co-injection of plasmid encoding HPS1 mutants defective in binding to HPS4 (L588P, RY and DV) were unable to rescue the melanin levels of *hps1* crispants (Fig. 7a, b). Similarly, the HPS4 $\Delta 675$ -686 mutant could not rescue the loss of melanin level of *hps4* crispants, suggesting that the BLOC-3 assembly is critical for melanogenesis in zebrafish (Fig. 7c, d). Notably, the HPS4 KR mutant that was deficient in RAB9A binding also failed to rescue the loss of melanin level in *hps4* crispants, indicating that HPS4-RAB9A interaction is indispensable for melanogenesis (Fig. 7c, d).

In addition to the CRISPR/Cas9 technology, we also depleted *hps4* using a splicing-blocking morpholino (MO), and these embryos displayed much severe phenotypes relative to *hps4* crispants (Supplementary Fig. 16a–c). Critically, co-injection of mRNA encoding human HPS4 WT, but not mutants ($\Delta 675$ -686 or KR), could partially rescue these defects (Supplementary Fig. 16a–c). Consistent with our immunoprecipitation results, HPS4 R185H or R268K rescued melanin levels as WT, indicating these variants are probably benign (Supplementary Fig. 16b, c). These findings collectively reveal that the interactions between HPS1-HPS4 and HPS4-RAB9A are essential for melanogenesis.

Discussion

The BLOC complexes are critical for the biogenesis of LROs, and mutations of genes encoding The BLOC complexes lead to HPS. One of the daunting tasks for clinicians and clinical scientists is to determine whether the genetic variants of HPS genes are benign or pathogenic^{10,11}. In this study, we reported the first cryo-EM structure of the BLOC complex, BLOC-3, and performed comprehensive studies characterizing the interaction between BLOC-3 and RAB32/38 or RAB9A. As our structure could readily explain the majority of pathogenic HPS1 and HPS4 variants (22 out of 24), our structural information provides a convenient strategy for the diagnosis of variants occurring on HPS1 or HPS4.

Our studies also identify a conserved catalytic mechanism utilized by TLD RabGEFs. All TLD RabGEF-associated RabGTPases harbor a Y[R/K] motif in their switch I, and this motif is often missing in other RabGTPases. Our structural modeling suggests that HPS1-HPS4 induces a conformational rearrangement in RAB32/38 surrounding the Y[R/K] motif, as Mon1-Ccz1 does in Ypt7. Importantly, we and others³⁰ have demonstrated that the Y[R/K] motif is critical for the GEF activity of TLD RabGEFs.

Conflicting data exist regarding the role of RAB9A in melanogenesis. While multiple studies reported that RAB9A is required for melanogenesis^{19,20}, likely via regulating the delivery of cargo to melanosomes, Ohishi et al.⁴⁷ found that the BLOC-3-RAB9A interaction was dispensable for melanogenesis in mammalian epidermal melanocytes. Our results are consistent with the former observation and support that the BLOC-3-RAB9A interaction is crucial in melanosome biogenesis in zebrafish. Consistent with this, Marubashi et al.¹⁹ also found that RUTBC1, another effector of RAB9A, was also essential for melanogenesis. Future research will be necessary to resolve the differences between these studies.

Our cryo-EM structure of BLOC-3 allows us to identify common and unique mechanisms in the TLD RabGEFs. TLD RabGEFs use analogous mechanisms to interact with and activate their respective substrates (Supplementary Fig. 12). Specifically, the interaction between TLD RabGEFs and their respective substrates predominantly involves a conserved pocket formed by two α -helices from the LD1 domains of TLD RabGEFs and the Y[R/K] motif of Rab GTPases (Supplementary Fig. 12). In contrast, TLD RabGEFs function as the effector of their corresponding Rab GTPases via distinct mechanisms (Supplementary Fig. 12). The CPLANE complex, via its subunit Fuzzy, interacts with the atypical small GTPase Rsg1²³. The interface comprises both LD1 and LD2 domains of Fuzzy and switch I, switch II, and the inter-switch region of Rsg1²³. Notably, the $\beta 3$ from the LD2 domain of Fuzzy LD2 and a β -strand from the inter-switch region of Rsg1 form a β -sheet²³. Importantly, a similar binding mode was predicted for the interface between yeast Mon1 and Ypt10, the yeast homolog of RAB5³⁵. In contrast, the counterpart of Fuzzy and Mon1 in BLOC-3, HPS1, is unlikely involved in binding to RAB9A. Furthermore, different from Fuzzy and Rsg1 (or Mon1 and Ypt10) that contact each other mainly by forming a β -sheet, HPS4 predominately relies on two α -helices (LD2- $\alpha 1$ and LD2- $\alpha 4$) to interact with RAB9A.

In summary, our study not only establishes the first high-resolution model of BLOC-3 but also lays a foundation for further understanding HPS pathogenic mutations in BLOC-3 and the development of potential therapeutic interventions.

Methods

Ethics

All experimental protocols were proved by the Animal Ethical Committee, West China Second University Hospital of Sichuan University.

Cloning, expression, and purification of proteins

Expression and purification of the BLOC-3 complex was modified from previous studies¹⁸. Briefly, the genes encoding N-terminal GST-tagged human HPS4 (residues 1–708 or $\Delta 289$ -518) and untagged human HPS1 (residues 1–700) were sub-cloned into the PH and p10 cassettes of the pFastBacDual vector (Invitrogen, Carlsbad, CA), respectively. SF9 cells were infected and incubated at 27 °C for 72 h before harvest. The cells were lysed in a buffer containing 50 mM HEPES, (pH 7.5), 150 mM NaCl, 1 mM PMSF, 1 mM DTT, 1 mM EDTA, and 5% (v/v) glycerol, then crushed using a high-pressure cell disrupter at 6 °C. Following high-speed centrifugation (43,000 $\times g$, 40 min), the supernatant was collected and incubated with Glutathione-Sepharose 4B beads (GE Healthcare) at 4 °C for 4 h. After washing and eluting, the proteins were further purified using Superdex 200 10/300 column (Cytiva) in a buffer containing 20 mM Tris-HCl, (pH 8.0) and 500 mM NaCl.

Similarly, Rab9A, RAB38, and RAB32 were expressed and purified as previously reported^{33,36}. In brief, mouse Rab9A (residues 2–199), human RAB38 (residues 2–211) and human RAB32 (residues 1–201) were sub-cloned into the pET-28a, pGEX-4T1 and pET-22a vectors (TSINGKE), respectively. All respective mutants were generated through site-directed mutagenesis. The recombinant protein was expressed in *Escherichia coli* BL21 (DE3) CodonPlus strain at 18 °C for 16 h after the addition of IPTG. His-tagged or GST-tagged proteins were captured by affinity chromatography using a Ni-NTA column (QIAGEN) or Glutathione-Sepharose beads (GE Healthcare) in the lysis buffer. Next, the eluted proteins were further purified by gel filtration chromatography using a Superdex 200 10/300 column (Cytiva) in a storage buffer (20 mM Tris-HCl, (pH 8.0), 2 mM MgCl₂, and 500 mM NaCl).

To get the BLOC-3-Rab9A complex, BLOC-3 and Rab9A Q66L were mixed at a 1:3 molar ratio in the storage buffer (20 mM Tris-HCl, (pH 8.0), 2 mM MgCl₂, and 500 mM NaCl) on ice for 1 h. The complex was then purified, followed by gel filtration chromatography using a Superdex 200 10/300 column (Cytiva) in a storage buffer (20 mM Tris-HCl, (pH 8.0), 2 mM MgCl₂, and 500 mM NaCl).

Cryo-EM sample vitrification and data collection

Cryo-EM sample was generated as described before⁴⁸. Briefly, three microliters of protein solution with 0.1 CMC Lauryl maltose neopentyl glycol (LMNG) were applied onto glow-discharged (60 s) M023-Au300-R1/1 grids (NanoDim Tech). The grids were blotted for 2–3 s and rapidly frozen in liquid ethane using a Vitrobot Mark IV (Thermo Fisher). Samples were loaded in a Titan Krios cryo-electron microscope (Thermo Fisher) operated at 300 kV in the following settings: condenser lens aperture 50 μm , spot size 6, magnification at $165,000\times$ (corresponding to a calibrated sampling of 0.85 \AA per physical pixel), and a K2 direct electron device equipped with a Bio-Quantum energy filter operated at 20 eV (Gatan). Movie stacks were collected automatically using EPU2 software (Thermo Fisher) with the K2 detector operating in counting mode at a recording rate of 5 raw frames per second and a total exposure time of 6 s, yielding 30 frames per movie stack and a total dose of 62.1 $\text{e}/\text{\AA}^2$.

Cryo-EM data processing

For BLOC-3, 10,755 movie stacks were imported in cryoSPARC 4.31 and subjected to Patch Motion Correction and Patch CTF Estimation⁴⁹. Micrographs were subjected to Blob Picker, and 1,118,353 particles were extracted. After 2D classification, selected particles were subjected to Topaz for model training. Topaz particle picking resulted in 862,907 particles⁵⁰. Subsequent 2D and 3D classifications, 3D auto-refinement, and Bayesian polishing resulted in 501,622 particles⁵¹, which were subjected to cryoSPARC ab initio and heterogeneous refinement. The resulting best 3D classes by visual examination were subjected to cryoSPARC local refinement, resulting in a final reconstruction at 3.2 \AA . The resolution was estimated by the FSC curve using the 0.143 criterion. The final density map was sharpened by DeepEMhancer⁵².

For BLOC-3-Rab9A, 11,110 movie stacks were imported in cryoSPARC 4.31 and subjected to Patch Motion Correction and Patch CTF Estimation⁴⁹. Micrographs were subjected to Topaz particle picking⁵⁰ and 851,793 particles were extracted. After two rounds of 2D classification and several rounds of ab initio and heterogeneous refinement, 271,048 particles complex were subjected to 3D Classification. The resulting best 3D classes by visual examination were subjected to cryoSPARC local refinement, resulting in a final reconstruction at 4.40 \AA . The resolution was estimated by the FSC curve using the 0.143 criterion. The final density map was sharpened by DeepEMhancer⁵². Details for data processing could be found in Supplementary Fig.11 and Table 1. To dock the RAB9A model, the final map was low-pass filtered to 8 \AA . Details for data processing could be found in Supplementary Figs.1 and 11 and Table 1.

Model building and refinement

The initial BLOC-3 complex model was generated by AlphaFold2³². The model was docked into the DeepEMhancer processed cryo-EM map in UCSF Chimera1.14⁵³, followed by iterative manual adjustment and real-space refinement using Coot 0.8.9.2 and Phenix 1.19^{54,55}, respectively. Statistics of the final models were provided in Table 1. Figures were prepared with UCSF ChimeraX1.110 and PyMOL⁵⁶. The data validation statistics are shown in Table 1.

AlphaFold modeling

The interaction models of HPS1-HPS4-RAB38 and HPS1-HPS4-RAB9A were generated using AlphaFold2 on the Google Colab platform or AlphaFold3 on the AlphaFold Server (<https://alphafoldserver.com/about>), respectively^{32,34}. For the HPS1-HPS4-RAB38 model, the sequences of HPS1 (residues 1–161), HPS4 (residues 1–172), and RAB38 (residues 1–181) were input into the query sequence module. Similarly, for the HPS1-HPS4-RAB9A-GTP model, the sequences of HPS1 (residues 1–700), HPS4 (residues 1–708), and RAB9A (residues 1–201) and GTP were used.

Cell culture and transfection

HEK293T and HEK293F cells were cultured in high-glucose Dulbecco's modified Eagles medium (DMEM), supplemented with penicillin-streptomycin 1% (v/v) (Hyclone) and 10% (v/v) fetal bovine serum (FBS) or FreeStyle™ 293 Expression Medium (Gibco), respectively^{57–60}. For HEK293F cells, 0.8 mg of the indicated plasmid was diluted in 40 ml of 293 F medium and mixed with 2.4 mg of polyethylenimine (PEI). This mixture was added to 800 ml of HEK293F cells at a density of 1.8×10^6 cells ml^{-1} . After 60 h of incubation at 37 °C, the cells were collected and centrifuged at $800\times g$ for 15 min. For HEK293T cells, the transfection mixture contained 9 μg of plasmid DNA and 27 μg PEI diluted in 0.5 ml of 293 T medium, respectively. The 1 ml mixture was carefully added to a 10 cm dish of HEK293T cells at a density of 70% to 80%. Following incubation for 24 h at 37 °C, the transfected HEK293T cells were centrifuged at $500\times g$ for 3 min.

Co-immunoprecipitation

HEK293T or HEK293F cells were first washed with PBS and lysed in a buffer consisting of 20 mM Tris-HCl, (pH 7.5), 150 mM NaCl, 2 mM MgCl_2 , and 1% Triton X-100 supplemented with protease inhibitors and 1 mM PMSF. The lysis process involved ultrasonication at 15% power, with ultrasound pulses lasting 3 s followed by 3 s pauses, totaling 2 min. Subsequently, the lysates were centrifuged at $12,000\times g$ for 10 min at 4 °C, and 5% of the supernatants were retained as lysate, while the remaining supernatants were utilized for immunoprecipitation. Immunoprecipitation was carried out for 2 h at 4 °C using anti-GFP Nanobody Magarose Beads or anti-Flag affinity beads. Following three washes with the lysis buffer, the beads were boiled in $2\times$ sample buffer. Separation was performed using SDS-PAGE, followed by analysis via immunoblotting with specified antibodies.

Guanine nucleotide exchange assay

The GEF assay for BLOC-3 was performed similarly to that of Mon1-Ccz1³⁰. Purified RAB32 and RAB38 were loaded with MANT-GDP (Jena Bioscience) overnight at 4 °C in the presence of 20 mM EDTA and 2 molar excess of fluorescent nucleotide. The loading reaction was terminated by adding MgCl_2 to a final concentration of 10 mM, and the resulting Rab GTPase-MANT-GDP complexes were purified via size exclusion chromatography in a buffer comprising 20 mM HEPES, (pH 7.5), 50 mM NaCl, 0.5 mM MgCl_2 , 1 mM DTT, and 10% (v/v) glycerol.

For the GEF activity assay, 2 μM Rab GTPase-MANT-GDP complexes were pre-incubated with indicated concentrations of the HPS1-HPS4 complex. The nucleotide exchange reaction was initiated by adding 200 μM GDP, and the substitution of MANT-GDP with GDP during GEF activity was monitored by observing the reduction in fluorescence emission at λ_{em} 488 nm (λ_{ex} 355 nm) at 30 °C at 15-second intervals. The data were fitted against a first-order exponential decay model ($y = y_0 + A \cdot \exp(-x/t)$), and k_{obs} was determined as $1/t$. Finally, k_{obs} was plotted against the concentration of HPS1-HPS4, and the catalytic efficiency (k_{cat}/K_M) in $\text{M}^{-1}\text{s}^{-1}$ was determined as the slope of the linear fit to the equation $y = A \cdot x + B$. The measured k_{obs} of the intrinsic nucleotide exchange rate served as a data point for 0 μM BLOC-3 concentration.

Zebrafish

All zebrafish (*Danio rerio*) experiments were performed according to standard procedures as previously described^{21,61,62}, and both adult fish and embryos were raised at 28.5 °C in Aquatic Ecosystems. AB strain (wild-type) was used in this study. Larvae were imaged at 4 days post-fertilization (dpf), a developmental stage at which sex is not yet distinguishable. All experimental protocols were proved by the Animal Ethical Committee, West China Second University Hospital of Sichuan University.

Preparation of RNP complex and microinjections

CRISPR/Cas9-mediated F0 gene knockout was performed as previously reported⁴⁶. Chemically synthesized *hps1*-specific and *hps4*-specific Alt-R® CRISPR-Cas9 crRNA (*hps1*: 5'-CACCATGGTGGACGACTCG-3', *hps4*: 5'-TAGTAGAGTCGATGGTCCTC-3') and universal Alt-R tracrRNA were purchased from Integrated DNA Technologies (IDT). A negative control crRNA (Alt-R® CRISPR-Cas9 Negative Control crRNA#1, 1072544) was also used. Duplex buffer (IDT) was utilized to resuspend the two RNA oligos into 100 µM stock solutions, which were subsequently stored at -20 °C. The 25 µM duplex crRNA:tracrRNA (dgRNA) was prepared by combining equal volumes of the two 100 µM RNA oligos with duplex buffer, following the annealing protocol: 95 °C for 5 min, cooling at 0.1 °C/sec to 25 °C, holding at 25 °C for 5 min, then rapid cooling to 4 °C, stored at -20 °C. A typical injection solution contained 1 µL of 25 µM crRNA:tracrRNA duplex, 1 µL of 25 µM Cas9 stock, and 2 µL nuclease-free H₂O (with the plasmids) to form the RNP complex. The injection dose for pCS2-mCherry plasmids containing the CMV promoter (Supplementary Table 1) was 15–30 pg per embryo. Microinjections were performed at the 1-cell stage embryos before cell inflation for all experiments.

Quantification indel frequencies in F0 crispant embryos

DNA from single embryos at 96 hpf was extracted. Embryos were digested in a mixture of 25 mM KOH and 0.2 mM EDTA (50 µL for 4 dpf embryos) at 95 °C for 30 min. Subsequently, the mixture was cooled and centrifuged, followed by neutralization with an equal volume of 40 mM Tris-HCl at pH 5. PCR reactions were performed from DNA extracted from each embryo, followed by Sanger sequencing analysis using the following primers. TIDE online software⁶³ (<https://tide.nki.nl/>) was used to determine the spectrum and frequency of targeted mutations.

hps1 Forward: 5'-CACTCATTATAAGCTCCCTGTTGT-3'
hps1 Reverse: 5'-TCAAACAGTATAATTCGTAAGCA-3'
hps4 Forward: 5'-ACATGAGCAGGACAGCTTCT-3'
hps4 Reverse: 5'-TGACAGCTATGGCATCTTTAAATTAAC-3'

Morpholino and mRNA injections

hps4 MO (5'-TATTGCAAGGCTTACATCTTCAGGA-3') and control MO (5'-CCTCTTACCTCAGTTACAATTTATA-3') were purchased from Gene Tools. *hps4* MO targets the third exon-intron junction and is designed to inhibit splicing. MO and mRNAs were injected into the yolk and the cell at the one-cell stage. The injection dose for *hps4* MO and control MO was 5 ng per embryo, with mRNA injection doses of 80–100 pg per embryo.

To determine the efficiency of MO, total RNAs of approximately 40 zebrafish embryos at 96 hpf were extracted as previously described⁶¹ and were then reverse transcribed to obtain cDNAs for use as Quantitative Real-time PCR (qPCR) templates. The qPCR assays were performed using a CFX96 real-time system (Bio-Rad), and the expression level of β-actin in zebrafish embryos was used as an internal control. The primer sequences used were as follows:

hps4 Forward: 5'-AGTTCAAAAGTGCAGGAGGAA-3'
hps4 Reverse: 5'-AGACGAACAGGAGATGAGGAC-3'
actin Forward: 5'-CGAGCAGGAGATGGGAACC-3'
actin Reverse: 5'-CAACGGAAACGCTCATTGC-3'

Melanin assay

Melanin levels were determined according to a previously published protocol⁴⁴. Briefly, larvae at 96 hpf from each group were combined and homogenized in 300 µL of homogenization buffer (20 mM Tris-HCl, (pH 7.5), 2 mM EGTA, 1 mM PMSF). Subsequently, homogenates were mixed with 500 µL of 2 M NaOH, 100 µL of DMSO, and 100 µL of ddH₂O, and incubated at 80 °C for 2 h. The mixture was then subjected to centrifugation, and the absorbance of the supernatant at 350 nm was measured using a microplate reader. Melanin levels were quantified using a standard curve.

Transmission electron microscopy

Zebrafish larvae at 96 hpf were fixed in 3% glutaraldehyde at 4 °C overnight, followed by postfixation in 1% OsO₄ for two hours. After washing with cacodylate buffer, the specimens were incubated in 1% uranyl acetate for one hour and then dehydrated in acetone. Subsequently, the dehydrating agent and Epon-812 embedding resin were sequentially infiltrated at ratios of 3:1, 1:1, and 1:3, followed by final embedding in Epon-812, and sectioned using an ultramicrotome (Leica). The sections were stained with uranyl acetate and lead citrate before examination with a JEM-1400FLASH electron microscope.

Statistical analysis

All statistical analyses were performed using GraphPad Prism 8. Data are presented as mean ± standard deviation (SD) or mean ± SEM. The normality of data distribution was assessed using the Shapiro-Wilk test. For normally distributed data, differences between groups were analyzed using one-way ANOVA followed by post hoc Tukey's test. Graphs and figures were generated using GraphPad Prism 8.

Reporting summary

Further information on research design is available in the Nature Portfolio Reporting Summary linked to this article.

Data availability

The structure factor and atomic coordinates of BLOC-3 were submitted to the Protein Data Bank under the ID code [8ZWC](#). In addition, the cryo-EM maps of BLOC-3 and the BLOC-3-Rab9A complex have been deposited in the Electron Microscopy Data Bank with the accession codes [EMD-60523](#) and [EMD-62821](#), respectively. The hyperlinks for the previously published PDB codes [8JBE](#), [7Q3D](#), [1SZI](#), [2LIG](#), and [5LDD](#) are as follows: [<https://www.rcsb.org/structure/8JBE>], [<https://www.rcsb.org/structure/7Q3D>], [<https://www.rcsb.org/structure/1SZI>], [<https://www.rcsb.org/structure/2LIG>], and [<https://www.rcsb.org/structure/5LDD>]. The source data underlying Figs. 1, 3–7, and Supplementary Figs. 8, 10, 11, 15, and 16 are provided in the Source Data file. Source data are provided in this paper.

References

- Bowman, S. L., Bi-Karchin, J., Le, L. & Marks, M. S. The road to lysosome-related organelles: Insights from Hermansky-Pudlak syndrome and other rare diseases. *Traffic* **20**, 404–435 (2019).
- Seward, S. L. Jr. & Gahl, W. A. Hermansky-Pudlak syndrome: health care throughout life. *Pediatrics* **132**, 153–160 (2013).
- Platt, F. M., d'Azzo, A., Davidson, B. L., Neufeld, E. F. & Tift, C. J. Lysosomal storage diseases. *Nat. Rev. Dis. Primers* **4**, 27 (2018).
- Wei, A. H. & Li, W. Hermansky-Pudlak syndrome: pigmentary and non-pigmentary defects and their pathogenesis. *Pigment Cell Melanoma Res.* **26**, 176–192 (2013).
- Li, W. et al. The BLOC interactomes form a network in endosomal transport. *J. Genet. Genomics* **34**, 669–682 (2007).
- Li, W. et al. Murine Hermansky-Pudlak syndrome genes: regulators of lysosome-related organelles. *Bioessays* **26**, 616–628 (2004).
- Huizing, M., Helip-Wooley, A., Westbroek, W., Gunay-Aygun, M. & Gahl, W. A. Disorders of lysosome-related organelle biogenesis: clinical and molecular genetics. *Annu. Rev. Genomics Hum. Genet.* **9**, 359–386 (2008).
- Dell'Angelica, E. C. The building BLOC(k)s of lysosomes and related organelles. *Curr. Opin. Cell Biol.* **16**, 458–464 (2004).
- Oh, J. et al. Mutation analysis of patients with Hermansky-Pudlak syndrome: a frameshift hot spot in the HPS gene and apparent locus heterogeneity. *Am. J. Hum. Genet.* **62**, 593–598 (1998).
- Huizing, M. et al. Hermansky-Pudlak syndrome: Mutation update. *Hum. Mutat.* **41**, 543–580 (2020).
- Li, W. et al. New insights into the pathogenesis of Hermansky-Pudlak syndrome. *Pigment Cell Melanoma Res.* **35**, 290–302 (2022).

12. Gerondopoulos, A., Langemeyer, L., Liang, J. R., Linford, A. & Barr, F. A. BLOC-3 mutated in Hermansky-Pudlak syndrome is a Rab32/38 guanine nucleotide exchange factor. *Curr. Biol.* **22**, 2135–2139 (2012).
13. Schuster, E. M. et al. TFEB induces mitochondrial itaconate synthesis to suppress bacterial growth in macrophages. *Nat. Metab.* **4**, 856–866 (2022).
14. Li, Y. et al. Analysis of the Rab GTPase interactome in Dendritic cells reveals anti-microbial functions of the Rab32 complex in bacterial containment. *Immunity* **44**, 422–437 (2016).
15. Balci, A., Solano-Collado, V., Baldassarre, M. & Spano, S. VARP and Rab9 are dispensable for the Rab32/BLOC-3 dependent salmonella killing. *Front. Cell Infect. Microbiol.* **10**, 581024 (2020).
16. Chen, M. et al. Itaconate is an effector of a Rab GTPase cell-autonomous host defense pathway against Salmonella. *Science* **369**, 450–455 (2020).
17. Baldassarre, M. et al. The Rab32/BLOC-3-dependent pathway mediates host defense against different pathogens in human macrophages. *Sci. Adv.* **7**, eabb1795 (2021).
18. Kloer, D. P. et al. Assembly of the biogenesis of lysosome-related organelles complex-3 (BLOC-3) and its interaction with Rab9. *J. Biol. Chem.* **285**, 7794–7804 (2010).
19. Marubashi, S., Shimada, H., Fukuda, M. & Ohbayashi, N. RUTBC1 Functions as a GTPase-activating protein for Rab32/38 and regulates melanogenic enzyme trafficking in melanocytes. *J. Biol. Chem.* **291**, 1427–1440 (2016).
20. Mahanty, S. et al. Rab9A is required for delivery of cargo from recycling endosomes to melanosomes. *Pigment Cell Melanoma Res.* **29**, 43–59 (2016).
21. Yong, X. et al. Cryo-EM structure of the Mon1-Ccz1-RMC1 complex reveals molecular basis of metazoan RAB7A activation. *Proc. Natl. Acad. Sci. USA* **120**, e2301725120 (2023).
22. Klink, B. U. et al. Structure of the Mon1-Ccz1 complex reveals molecular basis of membrane binding for Rab7 activation. *Proc. Natl. Acad. Sci. USA* **119**, e2121494119 (2022).
23. Langousis, G. et al. Structure of the ciliogenesis-associated CPLANE complex. *Sci. Adv.* **8**, eabn0832 (2022).
24. Herrmann, E. et al. Structure of the metazoan Rab7 GEF complex Mon1-Ccz1-Bul1. *Proc. Natl. Acad. Sci. USA* **120**, e2301908120 (2023).
25. Levine, T. P. et al. Discovery of new Longin and Roadblock domains that form platforms for small GTPases in Regulator and TRAPP-II. *Small GTPases* **4**, 62–69 (2013).
26. de Araujo, M. E. G. et al. Crystal structure of the human lysosomal mTORC1 scaffold complex and its impact on signaling. *Science* **358**, 377–381 (2017).
27. Hickenbottom, S. J., Kimmel, A. R., Londos, C. & Hurley, J. H. Structure of a lipid droplet protein; the PAT family member TIP47. *Structure* **12**, 1199–1207 (2004).
28. Choi, Y. M. et al. Structural insights into perilipin 3 membrane association in response to diacylglycerol accumulation. *Nat. Commun.* **14**, 3204 (2023).
29. Milburn, M. V. et al. Three-dimensional structures of the ligand-binding domain of the bacterial aspartate receptor with and without a ligand. *Science* **254**, 1342–1347 (1991).
30. Kiontke, S. et al. Architecture and mechanism of the late endosomal Rab7-like Ypt7 guanine nucleotide exchange factor complex Mon1-Ccz1. *Nat. Commun.* **8**, 14034 (2017).
31. Gerondopoulos, A. et al. Planar cell polarity effector proteins intermingle and form a Rab23 GEF complex. *Curr. Biol.* **29**, 3323–3330 (2019).
32. Jumper, J. et al. Highly accurate protein structure prediction with AlphaFold. *Nature* **596**, 583–589 (2021).
33. McGrath, E., Waschbusch, D., Baker, B. M. & Khan, A. R. LRRK2 binds to the Rab32 subfamily in a GTP-dependent manner via its armadillo domain. *Small GTPases* **12**, 133–146 (2021).
34. Abramson, J. et al. Accurate structure prediction of biomolecular interactions with AlphaFold 3. *Nature* **630**, 493–500 (2024).
35. Borchers, A. C. et al. Regulatory sites in the Mon1-Ccz1 complex control Rab5 to Rab7 transition and endosome maturation. *Proc. Natl. Acad. Sci. USA* **120**, e2303750120 (2023).
36. Zhang, Z., Wang, S., Shen, T., Chen, J. & Ding, J. Crystal structure of the Rab9A-RUTBC2 RBD complex reveals the molecular basis for the binding specificity of Rab9A with RUTBC2. *Structure* **22**, 1408–1420 (2014).
37. Arcot Sadagopan, K. et al. Cutaneous freckling: Possible new clinical marker for the diagnosis of Hermansky-Pudlak syndrome in Indian Asian patients with oculocutaneous albinism. *Ophthalmic Genet.* **38**, 194–196 (2017).
38. Lasseaux, E. et al. Molecular characterization of a series of 990 index patients with albinism. *Pigment Cell Melanoma Res.* **31**, 466–474 (2018).
39. Schenk, H. et al. Characterizing renal involvement in Hermansky-Pudlak Syndrome in a zebrafish model. *Sci. Rep.* **9**, 17718 (2019).
40. Hsu, C. C., Pai, W. Y., Lai, C. Y., Lu, M. W. & Her, G. M. Genetic characterization and in vivo image analysis of novel zebrafish Danio rerio pigment mutants. *J. Fish Biol.* **82**, 1671–1683 (2013).
41. Daly, C. M., Willer, J., Gregg, R. & Gross, J. M. snow white, a zebrafish model of Hermansky-Pudlak Syndrome type 5. *Genetics* **195**, 481–494 (2013).
42. Chen, T. et al. Development of the swimbladder surfactant system and biogenesis of Lysosome-related organelles is regulated by BLOS1 in Zebrafish. *Genetics* **208**, 1131–1146 (2018).
43. Thomas, J. L. et al. The loss of vacuolar protein sorting 11 (vps11) causes retinal pathogenesis in a vertebrate model of syndromic albinism. *Invest. Ophthalmol. Vis. Sci.* **52**, 3119–3128 (2011).
44. Maldonado, E., Hernandez, F., Lozano, C., Castro, M. E. & Navarro, R. E. The zebrafish mutant vps18 as a model for vesicle-traffic related hypopigmentation diseases. *Pigment Cell Res.* **19**, 315–326 (2006).
45. Schonthaler, H. B. et al. The zebrafish mutant lbk/vam6 resembles human multisystemic disorders caused by aberrant trafficking of endosomal vesicles. *Development* **135**, 387–399 (2008).
46. Hoshijima, K. et al. Highly efficient CRISPR-Cas9-based methods for generating deletion mutations and F0 Embryos that lack gene function in Zebrafish. *Dev. Cell* **51**, 645–657 (2019).
47. Ohishi, Y., Kinoshita, R., Marubashi, S., Ishida, M. & Fukuda, M. The BLOC-3 subunit HPS4 is required for activation of Rab32/38 GTPases in melanogenesis, but its Rab9 activity is dispensable for melanogenesis. *J. Biol. Chem.* **294**, 6912–6922 (2019).
48. Deng, H. et al. The WDR11 complex is a receptor for acidic-cluster-containing cargo proteins. *Cell* **187**, 4272–4288 (2024).
49. Punjani, A., Rubinstein, J. L., Fleet, D. J. & Brubaker, M. A. cryoSPARC: algorithms for rapid unsupervised cryo-EM structure determination. *Nat. Methods* **14**, 290–296 (2017).
50. Bepler, T. et al. Positive-unlabeled convolutional neural networks for particle picking in cryo-electron micrographs. *Nat. Methods* **16**, 1153–1160 (2019).
51. Zivanov, J. et al. New tools for automated high-resolution cryo-EM structure determination in RELION-3. *Elife* **7**, e42166 (2018).
52. Sanchez-Garcia, R. et al. DeepEMhancer: a deep learning solution for cryo-EM volume post-processing. *Commun. Biol.* **4**, 874 (2021).
53. Pettersen, E. F. et al. UCSF Chimera—a visualization system for exploratory research and analysis. *J. Comput. Chem.* **25**, 1605–1612 (2004).
54. Adams, P. D. et al. PHENIX: a comprehensive Python-based system for macromolecular structure solution. *Acta Crystallogr. D Biol. Crystallogr.* **66**, 213–221 (2010).
55. Emsley, P. & Cowtan, K. Coot: model-building tools for molecular graphics. *Acta Crystallogr. D Biol. Crystallogr.* **60**, 2126–2132 (2004).

56. Pettersen, E. F. et al. UCSF ChimeraX: Structure visualization for researchers, educators, and developers. *Protein Sci.* **30**, 70–82 (2021).
57. Shang, Z. et al. TRIM25 predominately associates with anti-viral stress granules. *Nat. Commun.* **15**, 4127 (2024).
58. Tu, Y. et al. TBC1D23 mediates Golgi-specific LKB1 signaling. *Nat. Commun.* **15**, 1785 (2024).
59. Chi, P. et al. Structural basis of the subcortical maternal complex and its implications in reproductive disorders. *Nat. Struct. Mol. Biol.* **31**, 115–124 (2024).
60. Qin, J. et al. Ketogenic diet reshapes cancer metabolism through lysine beta-hydroxybutyrylation. *Nat. Metab.* **6**, 1505–1528 (2024).
61. Zhao, L. et al. FAM91A1-TBC1D23 complex structure reveals human genetic variations susceptible for PCH. *Proc. Natl. Acad. Sci. USA* **120**, e2309910120 (2023).
62. Liu, Z. et al. SCGN deficiency is a risk factor for autism spectrum disorder. *Signal Transduct. Target. Ther.* **8**, 3 (2023).
63. Brinkman, E. K. et al. Easy quantification of template-directed CRISPR/Cas9 editing. *Nucleic Acids Res.* **46**, e58 (2018).

Acknowledgements

Cryo-EM data were collected on Can Cong at SKLB West China Cryo-EM Center and processed on Duyu High Performance Computing Center in Sichuan University. This work was supported by National Key Research and Development Program of China (2022YFA1105200, 2022YFC2303700 2021YFA1301900, 2024YFA1108500), Natural Science Foundation of China (NSFC, #92254302, #32200559, #32222040, #32430027, #32070049), National Science Fund for Distinguished Young Scholars (#32125012), Sichuan Science and Technology Program (#2024NSFSC1291, #2025NSFTD0028), China Postdoctoral Science Foundation (#2021M702364), “From 0 to 1” Innovation Research Project by Sichuan University (#2023SCUH0022), and a NIH grant (NIDDK DK10773).

Author contributions

X.Y. and D.J. conceived the project. X.Y. conducted biochemical experiments with assistance from C.Z. and Q.Y. performed the zebrafish studies. G.J. completed the cryo-EM analysis under the supervision of Z.S., S.Z., H.D., and D.D.B. contributed to the discussion. X.Y. and D.J. prepared the paper with input from all authors.

Competing interests

The authors declare no competing interests.

Additional information

Supplementary information The online version contains supplementary material available at <https://doi.org/10.1038/s41467-025-58235-1>.

Correspondence and requests for materials should be addressed to Zhaoming Su or Da Jia.

Peer review information *Nature Communications* thanks Robert Kelsh and the other anonymous reviewer(s) for their contribution to the peer review of this work. A peer review file is available.

Reprints and permissions information is available at <http://www.nature.com/reprints>

Publisher's note Springer Nature remains neutral with regard to jurisdictional claims in published maps and institutional affiliations.

Open Access This article is licensed under a Creative Commons Attribution-NonCommercial-NoDerivatives 4.0 International License, which permits any non-commercial use, sharing, distribution and reproduction in any medium or format, as long as you give appropriate credit to the original author(s) and the source, provide a link to the Creative Commons licence, and indicate if you modified the licensed material. You do not have permission under this licence to share adapted material derived from this article or parts of it. The images or other third party material in this article are included in the article's Creative Commons licence, unless indicated otherwise in a credit line to the material. If material is not included in the article's Creative Commons licence and your intended use is not permitted by statutory regulation or exceeds the permitted use, you will need to obtain permission directly from the copyright holder. To view a copy of this licence, visit <http://creativecommons.org/licenses/by-nc-nd/4.0/>.

© The Author(s) 2025